Nanoscale

COMMUNICATION

View Article Online
View Journal

Cite this: DOI: 10.1039/d6nr01480a

Received 15th April 2026,
Accepted 19th May 2026

DOI: 10.1039/d6nr01480a

rsc.li/nanoscale

Divergent phase evolution in mixed oxide $W_{0.5}Mo_{0.5}O_3$ under electron beam irradiation and thermal annealing

Naveen Goyal,*[a,b,c] Johannes Biskupek[b] and Ute Kaiser*[b,c]

Mixed metal oxides such as $W_{0.5}Mo_{0.5}O_3$ offer a unique platform for tailoring structural and electronic properties through the synergistic integration of tungsten and molybdenum oxides, yet their phase transformation pathway is poorly understood. Here, we investigate the real-time structural evolution of $W_{0.5}Mo_{0.5}O_3$ using advanced *in situ* transmission electron microscopy (TEM). By decoupling electron-beam irradiation from thermal annealing, two distinct transformation pathways are identified. Under continuous electron irradiation at ambient temperature, orthorhombic hydrated $W_{0.5}Mo_{0.5}O_3$ undergoes topotactic dehydration and transforms into a hexagonal phase before complete amorphization at a critical dose of 2.45 × 10^8 e^- nm^{-2} due to radiolysis. Conversely, *in situ* thermal annealing up to 1200 °C facilitates a controlled reduction process. While the initial dehydration mirrors the beam-induced pathway, elevated temperatures (>600 °C) trigger the nucleation of oxygen-deficient mixed-metal oxide phase. High-resolution TEM, STEM-EDS mapping and EELS analysis confirm the formation of an orthorhombic $Mo_2W_2O_{11}$ framework that maintains 1 : 1 W : Mo atomic ratio. Remarkably, this phase remains crystalline and unexpectedly stable at 1200 °C, far above the reported melting range of molybdenum oxides. These findings provide a quantitative framework for understanding radiation limits in 2D-layered oxides and offer a strategic route for synthesizing thermally robust metastable phases for electrochromic and energy-storage applications.

1. Introduction

Transition metal oxides such as WO_3 and MoO_3, are pivotal for electrochromic, gas sensing, and energy storage technologies due to their wide band gaps (2.5–3.0 eV) and versatile ion-hosting capabilities.[1–5] The functional properties of these oxides are highly phase-dependent; exemplified by the tetragonal WO_3 phase exhibiting twice the electrical conductivity of its counterpart monoclinic phase.[6] The phase of these materials is structurally sensitive to external stimuli, including temperature, pressure, and chemical precursors. For instance, solvothermal synthesis of WO_3 with or without oxalic acid yields orthorhombic or hexagonal phases,[7] respectively, while annealing in a hydrogen atmosphere can produce a variety of non-stoichiometric Magnéli phases (MO_{3-x}).[8,9] This diverse range of stoichiometric and non-stoichiometric phases allows these oxides to be tailored for a wide spectrum of functional applications.[10–12]

The incorporation of Mo into the WO_3 lattice provides an additional degree of freedom to modulate electronic properties, such as band gap reduction, thereby enhancing performance in solar water splitting, gas sensing, and supercapacitors.[13–16] The comparable ionic radii of Mo and W, and the isostructural nature of their hydrated phases, allow for complete substitutional flexibility across the entire mixed metal oxide composition range ($Mo_xW_{1-x}O_3$, x = 0–1).[17] However, despite extensive literature on individual WO_3 and MoO_3, the properties of their mixed-metal oxide counterparts remain less explored. To fully leverage the potential of $Mo_xW_{1-x}O_3$ materials, understanding their phase-transformation behaviour is a prerequisite, as the functional properties are a direct consequence of the underlying crystallographic structure.

The structural evolution of individual WO_3 and MoO_3 under thermal stimuli has been extensively documented, revealing complex phase transformation pathways.[18] In WO_3 systems, heating under high-vacuum typically proceeds either directly to metallic W or through a sequential transition to WO_2 *via* the intermediate $W_{18}O_{49}$ phase.[19–21] Similarly, MoO_3 reduction often follows two primary routes: direct conversion to metallic Mo or the formation of MoO_2 through an intermediate Mo_4O_{11} phase.[22–24] The nature of these transitions is highly sensitive to the initial phase and the specific external stimulus applied.[25] However, despite these insights into binary systems, to the best of our knowledge, the phase trans-

[a]*Collaborative Research Centre, Technical University Dresden, 01062, Germany. E-mail: naveen.goyal@mailbox.tu-dresden.de*
[b]*Electron Microscopy Group of Materials Science, University of Ulm, 89081, Germany. E-mail: ute.kaiser@uni-ulm.de*
[c]*Institute of Quantum Optics, University of Ulm, 89081, Germany*

formation behaviour of mixed-metal oxide $Mo_xW_{1-x}O_3$ remains elusive particularly under different stimuli.

To resolve these complexities, *in situ* transmission electron microscopy (TEM) has emerged as an indispensable technique, enabling the direct, real-time monitoring of phase transformations, nucleation events, and growth mechanisms at the atomic scale.[26,27] However, achieving accurate *in situ* observations requires a rigorous decoupling of thermal annealing effects from electron-beam interactions. Such decoupling is critical because high-energy electrons can induce unintended chemical changes through radiolysis or knock-on displacement, which may either compete or accelerate thermally driven transitions.[28,29]

In this work, we employ aberration-corrected *in situ* TEM to investigate the real-time phase transformation dynamics of the mixed-metal oxide $W_{0.5}Mo_{0.5}O_3$ by experimentally decoupling effects of electron beam with thermal annealing. We first demonstrate that electron-beam irradiation triggers a transition from the initial orthorhombic phase to a hexagonal structure *via* topotactic dehydration, followed by eventual amorphization. In contrast, *in situ* heating reveals a divergent pathway: the formation and unexpected stabilization of an oxygen-deficient Mo_4O_{11}-type phase at temperatures up to 1200 °C exceeding its melting point. This anomalous thermal stability is attributed to the stabilizing role of tungsten substitution and 90° grain boundaries. Our findings provide critical insights into the phase evolution of complex oxides, offering a potent strategy for tailoring material characteristics for next-generation electronics, catalysis, and energy storage.

2. Methods

Chemicals

$Na_2WO_4{\cdot}2H_2O$ (99%, SDFCL), $Na_2MoO_4{\cdot}2H_2O$ (99%, SDFCL), and HCl (34.5% liquid, SDFCL). All the chemicals have been utilized without additional purification.

Synthesis of $W_{0.5}Mo_{0.5}O_3$ nanostructures

The $W_{0.5}Mo_{0.5}O_3$ nanostructures were synthesized *via* a typical hydrothermal route.[14] In a representative procedure, equimolar amounts (1.25 mmol each) of $Na_2WO_4{\cdot}2H_2O$ and $Na_2MoO_4{\cdot}2H_2O$ were dissolved in 18 mL of deionized water. The precursor solution was acidified by the dropwise addition of 2 mL of HCl under constant magnetic stirring. After 20 minutes of vigorous agitation, the resulting mixture was transferred to a Teflon-lined stainless-steel autoclave and maintained at 120 °C for 24 hours. Upon completion of the reaction, the system was allowed to cool naturally to ambient temperature. The resulting precipitate was collected and purified through multiple washing cycles with deionized water and ethanol respectively. Finally, the obtained product was dried under vacuum.

Materials characterization

Structural transitions in $W_{0.5}Mo_{0.5}O_3$ induced by both electron-beam irradiation and *in situ* heating were investigated using an FEI Titan 80-300 transmission electron microscope (TEM) operated at an accelerating voltage of 300 kV. The microscope was equipped with an imaging-side CEOS hexapole corrector (C_s spherical aberration), enabling the correction of geometric axial aberrations up to the third order. Scanning transmission electron microscopy (STEM) combined with energy dispersive X-ray spectroscopy (EDS) mapping was performed on a Thermo Fisher Talos F200X instrument, equipped with a Super-X detector, operated at 200 kV. For electron-beam-induced phase transition studies, the $W_{0.5}Mo_{0.5}O_3$ nanostructures were dispersed in ethanol and drop-cast onto lacey carbon grids. *In situ* heating experiments were conducted using a Thermofisher Nano-Ex/iV heating holder that operates with MEMS chips. These chips featured 22 viewing windows encapsulated by a 15 nm-thick holey SiN_x membrane. The $W_{0.5}Mo_{0.5}O_3$ suspension was drop-cast directly onto the viewing windows. Thermal measurements were performed by heating the specimen up to 1200 °C at a constant ramp rate of 2 °C s^{-1}.

3. Results and discussion

We synthesized $W_{0.5}Mo_{0.5}O_3$ template nanostructures *via* a hydrothermal route to study their phase transformation behaviour. By employing equimolar amounts of Mo and W precursors, we obtained a pure orthorhombic phase having composition $W_{0.5}Mo_{0.5}O_3$ $0.33H_2O$ (JCPDS: 35-0270, lattice parameters: a = 7.34 Å, b = 12.59 Å and c = 7.70 Å) characterized by uniform nanobelt morphology, single crystallinity and uniform distribution of W and Mo with 1 : 1 atomic fraction (see details in SI, Fig. S1). This synthesized orthorhombic structure then served as the starting material for all subsequent phase-transformation experiments. To monitor these transformations in real time, we utilized C_s-corrected TEM operating at an accelerating voltage of 300 kV.

To isolate the influence of the electron beam from thermal annealing effects, the $W_{0.5}Mo_{0.5}O_3$ $0.33H_2O$ nanostructures were first examined under electron-beam irradiation at ambient temperature. High-resolution (HR) TEM images (Fig. 1a–c) illustrate the structural evolution over time under a constant dose rate of 2.72×10^5 e^- nm^{-2} s^{-1}. The initial orthorhombic phase transitioned into a hexagonal phase evidenced by the marked hexagonal tunnels in Fig. 1b followed by structural degradation into an amorphous state. The full series of HRTEM micrographs, acquired at intervals from 0 to 900 s, is provided in Fig. S2.

The corresponding fast Fourier transform (FFT) of these HRTEM micrographs (Fig. 1d–k) confirm the changes in crystal symmetry. The initial orthorhombic phase, viewed along the [001] zone axis with characteristic two-fold symmetry, gradually shifts to a hexagonal symmetry and can be completely matched with hexagonal phase (JCPDS: 33-1387, lattice parameters: a = 7.30 Å and c = 3.90 Å). This transformation occurs with a clear retention of orientation, suggesting a topotactic-like transition. Mechanistically, this process can be attributed to two continuous steps: the dehydration of $W_{0.5}Mo_{0.5}O_3$ $0.33H_2O$ to $W_{0.5}Mo_{0.5}O_3$ followed by the atomic rearrangement. As illustrated by the atomic models in Fig. S3,

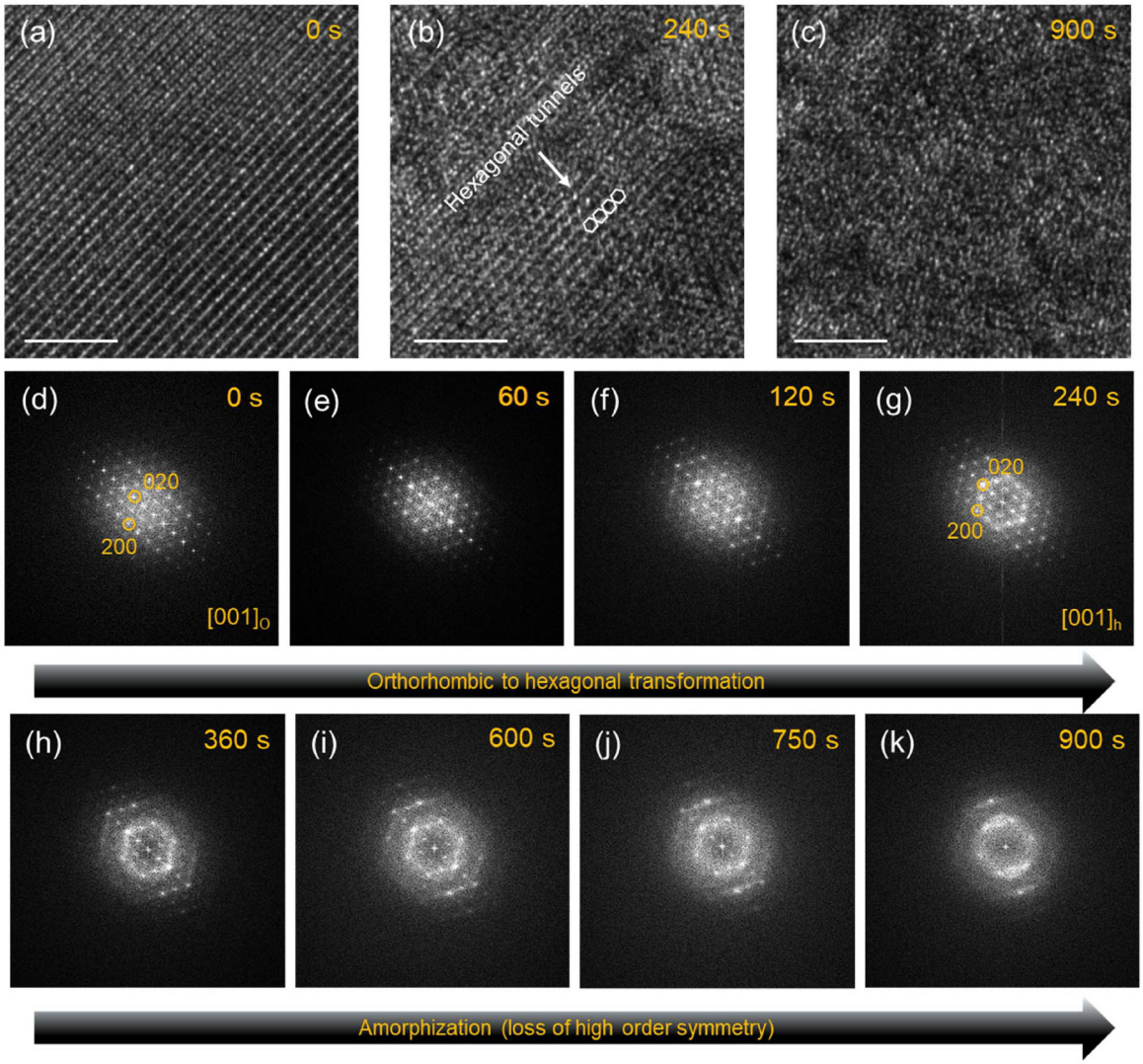

Fig. 1 Electron-beam-induced transformations in mixed metal oxide $W_{0.5}Mo_{0.5}O_3$ at a constant dose rate of 2.72×10^5 e^- nm^{-2} s^{-1}; (a–c) HRTEM images showing transformation of initial orthorhombic phase to hexagonal phase followed by structural degradation (scale bars are 5 nm); (d–k) series of FFTs obtained from the corresponding HRTEM images at regular interval of time depicting the change in symmetry/phase with effect of electron beam.

the transformation from the orthorhombic to hexagonal lattice can be understood as a shift of atomic columns by $a/2$ along the a-axis. This specific transformation pathway is favored because both the orthorhombic and hexagonal systems share nearly identical (001) planes and comparable lattice parameters along the a-direction, minimizing the interfacial strain during the phase shift.[25]

From a quantitative perspective, we determined the total electron dose required to induce the hexagonal phase as follows:

$$\begin{aligned}\text{Dose}_{\text{hexagonal}} &= \text{dose rate} \times \text{time} = (2.72 \times 10^5\ \text{e}^-\ \text{nm}^{-2}\ \text{s}^{-1}) \times (240\ \text{s}) \\ &= 6.53 \times 10^7\ \text{e}^-\ \text{nm}^{-2}\end{aligned}$$

The electron-beam-induced transition to a hexagonal phase is of particular interest for energy-storage applications; the characteristic open-tunnel framework of the hexagonal lattice provides low-resistance pathways that significantly enhance ion-intercalation kinetics in battery and electrochromic electrodes.[1,30–33]

Continued electron beam irradiation from 300 to 900 s resulted in gradual structural degradation, leading to complete amorphization (Fig. 1h–k), mostly due to radiolysis effect or Knotek–Feibelman (KF) mechanism.[34,35] The critical dose for the total degradation of $W_{0.5}Mo_{0.5}O_3$ is calculated to be:

$$\begin{aligned}\text{Dose}_{\text{critical}} &= \text{dose rate} \times \text{time} = (2.72 \times 10^5\ \text{e}^-\ \text{nm}^{-2}\ \text{s}^{-1}) \times (900\ \text{s}) \\ &= 2.45 \times 10^8\ \text{e}^-\ \text{nm}^{-2}\end{aligned}$$

An overview of the nanobelt morphology before and after irradiation is shown in Fig. S4.

The critical dose of 2.45×10^8 e^- nm^{-2} provides a quantitative benchmark for the radiation stability of $W_{0.5}Mo_{0.5}O_3$ under

high-energy electron irradiation. Overall, this electron-beam-induced transformation suggests that the phase of these mixed metal oxides can be precisely tuned at the nanoscale, offering a potential route for engineering high-performance components in next-generation electrochromic and energy-storage devices.

Next, *in situ* heating experiments were performed to evaluate the thermally induced phase transformation of $W_{0.5}Mo_{0.5}O_3$ using the same TEM operating at 300 kV. A single-tilt MEMS-based heating holder, featuring 22 independent viewing windows, was utilized for these experiments. The sample was prepared by dispersing the nanostructures onto the MEMS chip *via* drop-casting (Fig. S5). To ensure that the observed transitions were driven solely by thermal activation, the specimen was heated from room temperature to 1200 °C at a constant ramp rate of 2 °C s^{-1} while maintaining the electron beam in a 'blanked' state. At discrete intervals of 100 °C, the beam was unblanked to capture images at low magnification, thereby minimizing the cumulative electron dose and preventing beam-induced artifacts during the thermal study.

Fig. 2 presents low-magnification TEM images illustrating the morphological evolution of the nanostructures as a function of temperature. The initial nanobelt morphology of $W_{0.5}Mo_{0.5}O_3$ $0.33H_2O$ remains structurally intact up to 300 °C, with no noticeable changes observed (Fig. 2a–c). However, at 400 °C, small voids/vacancies begin to emerge as marked in Fig. 2d–f, which continued till 600 °C. The generation of this internal porosity can be attributed to the dehydration of the $W_{0.5}Mo_{0.5}O_3$ $0.33H_2O$ framework. This aligns with previous reports suggesting that the removal of structural water molecules typically require temperature around 300–350 °C.[14] From 700 °C to 1200 °C (Fig. 2g–l), the nanobelt morphology undergoes significant disruption, eventually fragmenting into discrete nano crystallites at 1200 °C. This morphological breakdown may stem from either a definitive phase transformation or cumulative structural degradation.

To precisely identify the evolution of the crystal structure, *in situ* selected area electron diffraction (SAED) patterns were acquired from the same individual nanocrystal at each temperature interval shown in Fig. 3. The initial SAED pattern (Fig. 3a) corresponds to the orthorhombic phase indexed along the [001] zone axis, confirming the single-crystalline nature of the $W_{0.5}Mo_{0.5}O_3$ $0.33H_2O$ nanobelt. Up to 300 °C, the crystal phase and orientation remain unchanged, consistent with the morphological observations. However, at 300 °C, a non-uniformity in the diffraction spot intensities is observed (marked in Fig. 3b), signalling the onset of a structural transition that becomes fully evident at 400 °C.

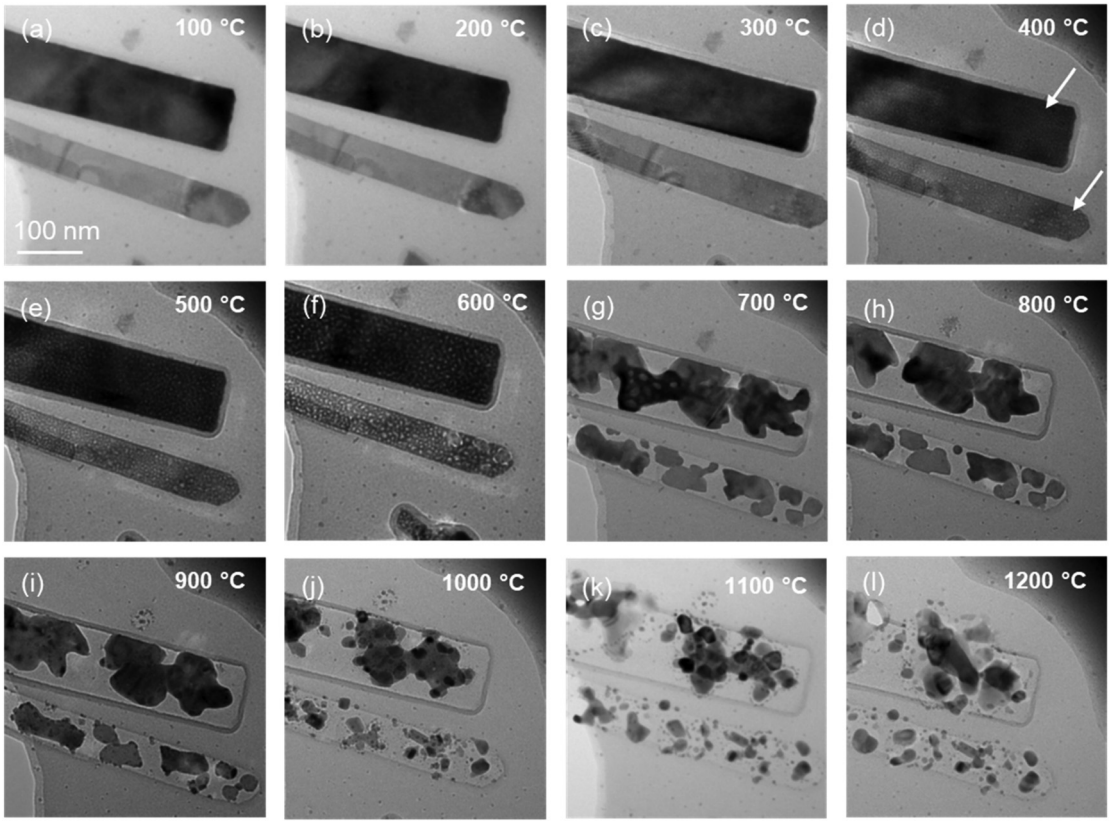

Fig. 2 Series of TEM images showing the morphological evolution of $W_{0.5}Mo_{0.5}O_3$ nanobelts during *in situ* heating with temperatures ranging from 100–1200 °C; (a–c) preservation of original nanobelt morphology; (d–f) appearance of small voids throughout the nanobelt; (g–l) disruption of nanobelt morphology to small crystallites (scale bar is identical in all the TEM images).

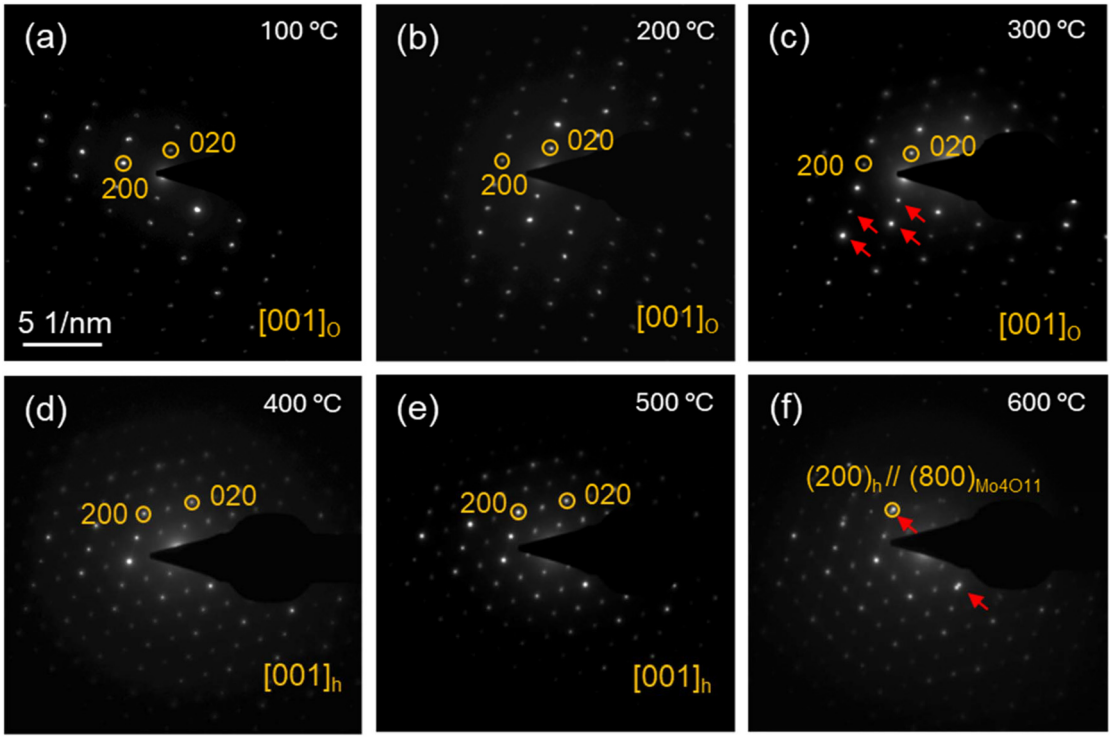

Fig. 3 Series of SAED patterns taken during *in situ* heating of $W_{0.5}Mo_{0.5}O_3$ with temperature ranging from 100–600 °C; (a–c) SAED pattern corresponds to orthorhombic phase of hydrated $W_{0.5}Mo_{0.5}O_3$ (red arrow shows variation in intensity of spots); (d and e) SAED pattern corresponds to hexagonal phase, (f) SAED pattern corresponding to hexagonal phase shows additional spots due to appearance of new oxygen deficient phase Mo_4O_{11} at 600 °C.

At 400 °C, a distinct phase transformation from orthorhombic to hexagonal is observed. The resulting SAED pattern exhibits characteristic six-fold symmetry, matching the hexagonal phase of $W_{0.5}Mo_{0.5}O_3$ (JCPDS no. 33-1387) while maintaining the original crystallographic orientation. This topotactic-like transition clarifies the appearance of the vacancies observed in the BF-TEM micrograph (Fig. 2d), which originate from the loss of structural water molecules.

This hexagonal phase persists up to 600 °C, as corroborated by the SAED pattern in Fig. 3f. Notably, at 600 °C, additional diffraction spots corresponding to the reduced oxide phase, Mo_4O_{11}, emerge alongside the hexagonal reflections. This indicates the initiation of a reduction process in the mixed-metal oxide, likely driven by the high vacuum environment of the TEM column, this observation aligns with previous *in situ* reports on individual WO_3 and MoO_3 systems.[19,20,22,24] Interestingly, the Mo_4O_{11} phase appears to grow epitaxially on the hexagonal $W_{0.5}Mo_{0.5}O_3$, with an epitaxial relationship as $(200)_{W_{0.5}Mo_{0.5}O_3}//(800)_{Mo_4O_{11}}$. Between 700 °C and 1100 °C, the growth of the oxygen-deficient Mo_4O_{11} phase was observed. The SAED patterns acquired within this temperature range correspond to the high-index zone axes of Mo_4O_{11} (JCPDS no. 01-073-1538, lattice parameters: a = 24.4 Å, b = 5.45 Å and c = 6.70 Å) (Fig. S6). Consequently, the previously noted structural disruption, where the nanobelt morphology fragments into discrete nano crystallites (Fig. 2g–l) can be directly attributed to the nucleation and growth of the Mo_4O_{11} phase.

Fig. 4 presents structural characterization of the reduced phase at 1200 °C. Fig. 4a and b shows TEM micrographs of Mo_4O_{11} crystallites at different magnification. The FFTs obtained from two distinct regions in Fig. 4b (shown in Fig. 4c and d) were indexed to the $[0\bar{1}1]$ zone axis of the orthorhombic Mo_4O_{11} phase (JCPDS no. 01-073-1538). Fig. 4e present HRTEM micrograph of Mo_4O_{11} along $[0\bar{1}1]$ zone axis with a sharp 90° grain boundaries between two Mo_4O_{11} crystallites.

The stability of the Mo_4O_{11} phase with high-crystallinity at 1200 °C is both remarkable and unexpected, as the reported melting range for this phase typically lies between 700–850 °C.[36,37] Under the high-vacuum conditions of the TEM, such oxides are typically expected to reduce further to metallic Mo; however, no prior reports mention the existence of Mo_4O_{11} structure at these extreme temperatures.[22,23] Furthermore, while the structural analysis strongly matches the Mo_4O_{11} lattice, the fate of the W atoms remained unclear.

To resolve the elemental distribution and quantify the W : Mo ratio, STEM-EDS mapping was performed on the 1200 °C product. The STEM-EDS maps (Fig. S7) reveal a co-existence of W and Mo throughout the sample, maintaining a consistent 1 : 1 atomic fraction. The preservation of this equimolar ratio throughout entire heating indicates the formation

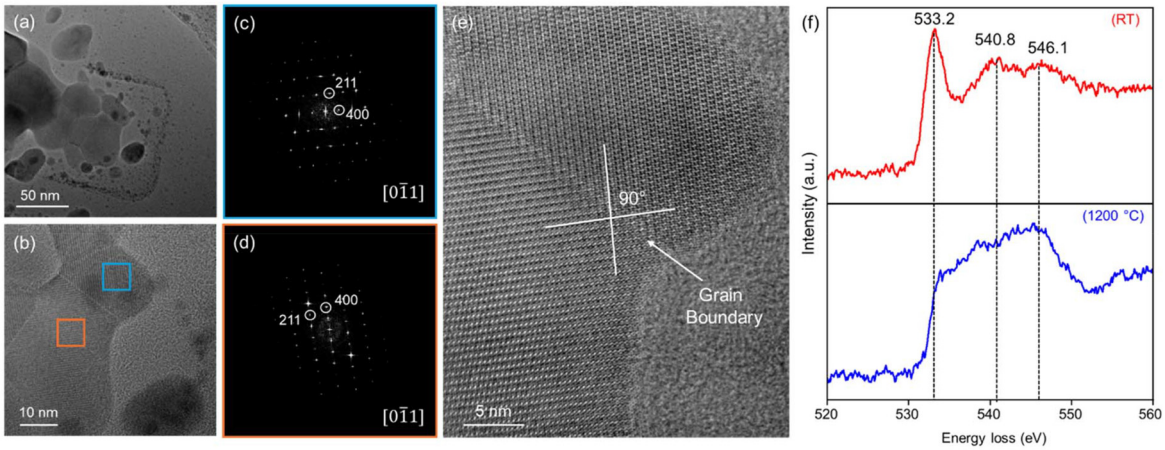

Fig. 4 Microstructural characterization of final product obtained at 1200 °C post heating; (a and b) TEM images at different magnification showcasing formation of irregular-shaped crystallites from the nanobelts of $W_{0.5}Mo_{0.5}O_3$; (c and d) FFTs taken from two different regions in (b); both corresponds to [0$\bar{1}$1] zone axis of Mo_4O_{11}; (e) HRTEM image of Mo_4O_{11} demonstrating a distinctive 90° grain boundary between two nano crystallites; (f) O–K edge EELS spectrum of the pristine sample at RT and product obtained at 1200 °C.

of a highly stable, reduced mixed-metal oxide phase, which can be identified as a substituted $Mo_2W_2O_{11}$ framework. Notably, the presence of distinct 90° grain boundaries between the $Mo_2W_2O_{11}$ crystallites (Fig. 4e) suggests a coordinated growth mechanism that might accommodates any lattice strain induced by W-substitution. This structural configuration, combined with the chemical influence of tungsten, likely provides the enhanced thermal and structural stability observed at 1200 °C, preventing the expected melting and further reduction of the oxide framework.

Next, EELS analysis was performed in the range 380–580 eV to capture the signals of Mo $M_{2,3}$ edges and O–K edges to determine changes in the oxidation states before and after heating of the samples (Fig. S8). The EELS O–K edge spectra provide compelling evidence for the chemical transformation from the hydrated $Mo_{0.5}W_{0.5}O_3$ to the $Mo_2W_2O_{11}$ phase. The O–K edge spectra of hydrated $Mo_{0.5}W_{0.5}O_3$ exhibits a fine structure characterized by three peaks (Fig. 4f), corresponding to transitions into well-defined t_{2g} and e_g hybridized states within a symmetric octahedral environment.[38,39] Upon reduction at 1200 °C, a transition to a single, broad hump is observed. This broadening is attributed to the increased structural complexity of the $Mo_2W_2O_{11}$ phase, which incorporates a variety of Mo/W–O coordination including edge-sharing and tetrahedral sites, leading to a distribution of hybridized state energies. Furthermore, the significant decrease in the O–K edge/peak intensity strongly supports the reduction of the metal centres.[38] As oxygen vacancies are formed, the resulting increase in d-orbital occupancy reduces the density of available states for O 1s to 2p transitions. This combination of ELNES broadening and intensity drop is a characteristic signature of the formation of the sub-stoichiometric $Mo_2W_2O_{11}$ framework.

Further, EELS data acquired in the range of 390–420 eV (Fig. S8) shows overlap between the Mo $M_{2,3}$ edges from sample and the N K-edges from the SiN_x support membrane. To mitigate substrate contributions, spectra were collected near the specimen edge (vacuum side) of the holey SiN_x-membrane of the MEMS chip. In the parent hydrate phase, the Mo $M_{2,3}$ region exhibits three distinct features, reflecting the well-defined crystal field splitting of Mo^{6+} in an octahedral environment.[39] Upon heating to 1200 °C, the transition to a two-hump profile is observed. This change could be interpreted as the formation of the $Mo_2W_2O_{11}$ phase introduces MoO_4 tetrahedra and distorted MoO_6 octahedra, resulting in a broader distribution of hybridized electronic states and partial merging of the fine-structure features. This evolution of the Mo M-edge complements the reduction in O K-edge intensity and together provides additional spectroscopic evidence consistent with the formation of the oxygen-deficient $Mo_2W_2O_{11}$ phase.

From *in situ* thermal annealing experiments, we conclude that initial $W_{0.5}Mo_{0.5}O_3$ $0.33H_2O$ first converted to hexagonal $W_{0.5}Mo_{0.5}O_3$ at 400 °C followed by $Mo_2W_2O_{11}$ starting from 700 °C. While the electron beam was in blanked state during temperature rise in the thermal annealing experiment except at discrete intervals of 100 °C, to capture TEM images at low magnification, additional experiment was performed to observe the coupling effects of electron beam and thermal annealing (Fig. S9), where the employment of electron beam irradiation of selected region (marked in Fig. S9b–d) leads to structure degradation and prevent the region for further transformation to oxygen vacant $Mo_2W_2O_{11}$ on increasing temperature. The time-resolved electron beam-induced effects on the marked region (Fig. S9b and c) of $Mo_{0.5}W_{0.5}O_3$ at 400 °C is presented in Fig. S10. The hexagonal $Mo_{0.5}W_{0.5}O_3$ formed at 400 °C during thermal annealing is electron beam irradiated for 600 s with a constant dose rate of 2.5×10^6 e^- nm^{-2} s^{-1}. As shown in Fig. S10, progressive loss of high-order symmetry and fading of diffraction spots are observed, consistent with beam-induced structural degradation mechanisms similar to those observed under room-temperature irradiation.

Furthermore, we performed an additional time-resolved electron-beam irradiation experiment at 700 °C on the oxygen-deficient $Mo_2W_2O_{11}$ phase (Fig. S11). The structure was continuously irradiated for 600 s at a dose rate of 4.8×10^6 $e^- nm^{-2} s^{-1}$. Under continuous irradiation, progressive structural degradation and reduction in crystallinity were observed, consistent with beam-induced damage processes similar to those identified at room temperature and 400 °C. Additionally, we compared the critical electron dose required for structural degradation in all three phase (Table 1) and found that oxygen-deficient $Mo_2W_2O_{11}$ phase exhibits significantly enhanced resistance to electron-beam induced degradation, showing the highest critical dose among the investigated phases, even at 700 °C.

To complement these findings, we performed density functional theory calculations (see SI for computational details) which yielded a formation energy of −31.98 eV for $Mo_2W_2O_{11}$. The structure model was constructed by random substitution of half of Mo atoms from Mo_4O_{11} with W atoms (Fig. S12). The calculated formation energy is comparable to that of pristine Mo_4O_{11} (−35.38 eV), suggesting that the mixed-metal phase is energetically favourable. It is important to note that the formation of $Mo_2W_2O_{11}$ phase in this study is governed by the 1 : 1 Mo : W ratio of the precursor $Mo_{0.5}W_{0.5}O_3$.

Fig. 5 summarizes the bifurcated phase-transformation pathways of $W_{0.5}Mo_{0.5}O_3$ $0.33H_2O$ under electron-beam irradiation and *in situ* thermal annealing. In both cases, the initial transformation stage appears consistent, proceeding *via* topotactic dehydration followed by a transition to the hexagonal $W_{0.5}Mo_{0.5}O_3$ phase. However, the subsequent evolution diverges significantly based on the stimulus. Under continuous electron-beam irradiation, radiolysis effects lead to rapid structural degradation. In contrast, *in situ* heating facilitates a controlled reduction process, culminating in the formation of a previously unreported, thermally stable mixed-metal oxide phase, $Mo_2W_2O_{11}$. This comparative study provides critical real-time insights into the phase dynamics of complex mixed-metal oxides. Furthermore, it demonstrates a precise methodology for synthesizing high-temperature phases, which are essential for advancing applications in electrochromic devices, gas sensing, and high-capacity battery electrodes.

Table 1 Comparison of critical dose of all three phases formed during *in situ* thermal annealing

Phase	Temperature (°C)	Critical dose ($e^- nm^{-2}$)
$Mo_{0.5}W_{0.5}O_3$ $0.33H_2O$	RT	2.45×10^8
$Mo_{0.5}W_{0.5}O_3$	400	1.5×10^9
$Mo_2W_2O_{11}$	700	2.88×10^9

4. Conclusion

In summary, this study provides a real-time analysis of the structural evolution in mixed-metal oxide $W_{0.5}Mo_{0.5}O_3$ under two distinct energetic stimuli. We demonstrate that ambient-temperature electron-beam irradiation triggers a topotactic orthorhombic-to-hexagonal transformation *via* dehydration and atomic rearrangement, eventually leading to radiolysis-induced amorphization. In contrast, *in situ* heating facilitates a controlled reduction process, culminating in the nucleation and growth of a reduced mixed-metal oxide phase, identified as $Mo_2W_2O_{11}$. Remarkably, this phase exhibits anomalous thermal stability, remaining crystalline at 1200 °C, significantly exceeding the typical stability range of molybdenum oxides. This enhanced stability is attributed to a combination of tungsten substitution and the formation of characteristic 90° grain boundaries, which effectively accommodate interfacial strain during high-temperature crystallization.

These findings demonstrate how decoupling electron-beam and thermal annealing effects in TEM enables direct insight into phase evolution in complex oxides. The ability to engineer

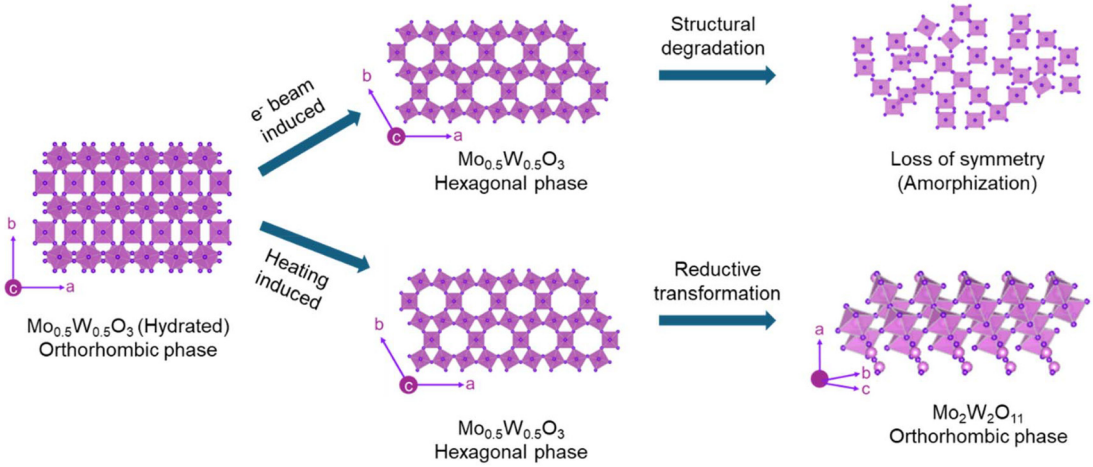

Fig. 5 Schematic summarizing the phase transformation pathways in $W_{0.5}Mo_{0.5}O_3$ under two distinct energetic stimuli in the TEM: electron-beam irradiation and *in situ* heating.

hexagonal tunnel structures and thermally robust mixed-metal oxide phases provides new opportunities for electrochromic devices, catalytic systems, and high-rate energy-storage materials. Furthermore, the identified electron-beam sensitivity offers a pathway for precision defect engineering and nanoscale patterning.

Author contributions

Naveen Goyal: conceptualization, supervision, investigation, data curation, methodology, formal analysis, writing – original draft, and writing – review & editing. Johannes Biskupek: investigation, data curation, writing – review & editing. Ute Kaiser: writing – review & editing, resources, supervision, and funding acquisition.

Conflicts of interest

The authors declare no competing financial interest.

Data availability

The data supporting this article have been included as part of the supplementary information (SI). Supplementary information is available. See DOI: https://doi.org/10.1039/d6nr01480a.

Acknowledgements

N. G. and U. K. acknowledges financial support from the German Research Foundation (DFG) under CRC 1415 (Chemistry of Synthetic Two-Dimensional Materials, no. 417590517). N. G. thanks Prof. N. Ravishankar, Indian Institute of Science (IISc) for providing wet-chemical laboratory for synthesis of nanostructures. N. G. acknowledges Pragyan Tripathi and Prof. Abhishek Singh (MRC, IISc) for their help in DFT calculations and fruitful discussions.

References

1 J. Besnardiere, B. Ma, A. Torres-Pardo, G. Wallez, H. Kabbour, J. M. González-Calbet, H. J. Von Bardeleben, B. Fleury, V. Buissette, C. Sanchez, T. Le Mercier, S. Cassaignon and D. Portehault, *Nat. Commun.*, 2019, **10**, 327.
2 W.-J. Li and Z.-W. Fu, *Appl. Surf. Sci.*, 2010, **256**, 2447–2452.
3 M. J. Priya, P. P. Subha, A. Antony, M. K. Jayaraj and K. Rajeev Kumar, *Chem. Phys. Lett.*, 2023, **829**, 140749.
4 J. Guo, H. Jia, Z. Shao, P. Jin and X. Cao, *Acc. Mater. Res.*, 2023, **4**, 438–447.
5 Y. He, M. Gu, H. Xiao, L. Luo, Y. Shao, F. Gao, Y. Du, S. X. Mao and C. Wang, *Angew. Chem., Int. Ed.*, 2016, **55**, 6244–6247.
6 R. S. Vemuri, K. K. Bharathi, S. K. Gullapalli and C. V. Ramana, *ACS Appl. Mater. Interfaces*, 2010, **2**, 2623–2628.
7 K. Ghosh, A. Roy, S. Tripathi, S. Ghule, A. K. Singh and N. Ravishankar, *J. Mater. Chem. C*, 2017, **5**, 7307–7316.
8 J. Cao, J. Xia, X. Li, Y. Li, P. Liu, L. Tian, P. Qiao, C. Liu, Y. Wang and X. Meng, *Small*, 2023, **19**, e2302365.
9 Y.-J. Lee, T. Lee and A. Soon, *Chem. Mater.*, 2019, **31**, 4282–4290.
10 I. A. de Castro, R. S. Datta, J. Z. Ou, A. Castellanos-Gomez, S. Sriram, T. Daeneke and K. Kalantar-Zadeh, *Adv. Mater.*, 2017, **29**, 1701619.
11 Y. Yao, D. Sang, L. Zou, Q. Wang and C. Liu, *Nanomaterials*, 2021, **11**, 2136.
12 M. G. da Silva Júnior, L. C. C. Arzuza, H. B. Sales, R. M. da C. Farias, G. de A. Neves, H. de L. Lira and R. R. Menezes, *Materials*, 2023, **16**, 7657.
13 D. Zhou, F. Shi, D. Xie, D. H. Wang, X. H. Xia, X. L. Wang, C. D. Gu and J. P. Tu, *J. Colloid Interface Sci.*, 2016, **465**, 112–120.
14 N. Goyal, G. Raj, K. K. Nanda and R. Narayanan, *J. Mater. Chem. C*, 2025, **13**, 6678–6692.
15 L. Han, Y. Liu, C. Chang, M. Liu, Z. Peng and F. Gong, *Chem. Phys. Lett.*, 2022, **794**, 139500.
16 S. S. Kalanur and H. Seo, *J. Colloid Interface Sci.*, 2018, **509**, 440–447.
17 L. Zhou, J. Zhu, M. Yu, X. Huang, Z. Li, Y. Wang and C. Yu, *J. Phys. Chem. C*, 2010, **114**, 20947–20954.
18 N. Goyal, R. K. Rai and N. Ravishankar, *Microsc. Microanal.*, 2024, **30**, ozae044.579.
19 M. Ahmadi, S. Sahoo, R. Younesi, A. P. S. Gaur, R. S. Katiyar and M. J.-F. Guinel, *J. Mater. Sci.*, 2014, **49**, 5899–5909.
20 K. Bao, Y. Ma, J. Tang and W. Liu, *Mater. Res. Lett.*, 2026, **14**, 169–175.
21 S. P. Gupta, H. H. Nishad, S. D. Chakane, S. W. Gosavi, D. J. Late and P. S. Walke, *Nanoscale Adv.*, 2020, **2**, 4689–4701.
22 W. Tu, F. Zhang, X. Song, L. Jin, A. Bai, Z. Zeng, T. Xu, X. Sun, Y. Yang and J. Huang, *Nano Lett.*, 2025, **25**, 13926–13934.
23 J. Chen and Q. Wei, *Int. J. Appl. Ceram. Technol.*, 2017, **14**, 1020–1025.
24 X. Chen, R. M. de Boer, A. Kosari, H. van Gog and M. A. van Huis, *J. Phys. Chem. C*, 2023, **127**, 21387–21398.
25 M. Figlarz, *Prog. Solid State Chem.*, 1989, **19**, 1–46.
26 Y. Li, F. Börrnert, M. Ghorbani-Asl, J. Biskupek, X. Zhang, Y. Zhang, D. Bresser, A. V. Krasheninnikov and U. Kaiser, *Adv. Funct. Mater.*, 2024, **34**, 2406034.
27 N. Li, X. Li, T. Wang, B. Wen, Z. Yin, J. Feng, S. Yang, Y. Yang, G. Yang and S. Ding, *Chem. Sci.*, 2025, **16**, 9604–9637.

28 Q. Chen, C. Dwyer, G. Sheng, C. Zhu, X. Li, C. Zheng and Y. Zhu, *Adv. Mater.*, 2020, **32**, 1907619.
29 S. Stangebye, Y. Zhang, S. Gupta, T. Zhu, O. Pierron and J. Kacher, *Acta Mater.*, 2022, **222**, 117441.
30 K. Huang and Q. Zhang, *Nano Energy*, 2012, **1**, 172–175.
31 X. Chen, R. Huang, M. Ding, H. He, F. Wang and S. Yin, *ACS Appl. Mater. Interfaces*, 2022, **14**, 3961–3969.
32 A. Tariq, M. D. Ghouri, K. Amin, M. Hamza, B. Khan and B. Wang, *ACS Appl. Energy Mater.*, 2025, **8**, 17033–17042.
33 D. Sachdeva, N. Goyal, M. Gayen and N. Ravishankar, *Chem. Mater.*, 2025, **37**, 5547–5557.
34 T. Lehnert, O. Lehtinen, G. Algara-Siller and U. Kaiser, *Appl. Phys. Lett.*, 2017, **10**, 033106.
35 D. Mücke, I. Cooley, B. Liang, Z. Wang, S. Park, R. Dong, X. Feng, H. Qi, E. Besley and U. Kaiser, *Nano Lett.*, 2024, **24**, 3014–3020.
36 Y. Qing, K. Yang, Y. Chen, J. Zhu, Y. Li, C. Chen, Q. Li, B. Sun and J. He, *Materials*, 2023, **16**, 2841.
37 M. Zoller, R. Bubnova, Y. Biryukov, E. Haussühl, R. Pöttgen, O. Janka, S. Penner, C. Praty, H. Fitzek, J. Winkler, S. Filatov and H. Huppertz, *Z. Kristallogr. – Cryst. Mater.*, 2020, **235**, 143–155.
38 F. Zhang, Y. Zhang, L. Li, X. Mou, H. Peng, S. Shen, M. Wang, K. Xiao, S.-H. Ji, D. Yi, T. Nan, J. Tang and P. Yu, *Nat. Commun.*, 2023, **14**, 3950.
39 L. Lajaunie, F. Boucher, R. Dessapt and P. Moreau, *Ultramicroscopy*, 2015, **149**, 1–8.